Interface engineering of high efficiency perovskite solar cells based on ZnO nanorods using atomic layer deposition

Shibin Li[1,] *(✉), Peng Zhang[1], Yafei Wang[1], Hojjatollah Sarvari[2], Detao Liu[1], Jiang Wu[3], Yajie Yang[1], Zhiming Wang[4], Zhi David Chen[1,2,] *(✉)

[1]School of Optoelectronic Information, University of Electronic Science and Technology of China (UESTC), Chengdu, 610054, China

[2]Department of Electrical & Computer Engineering and Center for Nanoscale Science &Engineering,
University of Kentucky,
Lexington, Kentucky 40506, USA

[3]Department of Electronic and Electrical Engineering, University College London, Torrington Place, London WC1E 7JE, United Kingdom

[4]Institute of Fundamental and Frontier Sciences, University of Electronic Science and Technology of China, Chengdu, 610054, China

ABSTRACT

Despite dramatically improved efficiency of inorganic-organic metal hybrid perovskite solar cells (PSCs), electron transport is still a challenging issue. In this paper, we report the use of ZnO nanorods prepared by hydrothermal self-assembly as the electron transport layer in perovskite solar cells. The efficiency of perovskite solar cells is dramatically enhanced by passivating the interface defects via atomic layer deposition of Al_2O_3 monolayers on ZnO nanorods. By employing Al_2O_3 monolayers, the power conversion efficiency (PCE) of $CH_3NH_3PbI_3$ (MAPbI$_3$) PSCs is typically boosted from 10.33% to 15.06% on average, with the highest efficiency of 16.08%. We suggest that passivation of defects using atomic layer deposition of monolayers might provide a new pathway for improving all types of PSCs.

1 Instruction

Although sunlight is a clean, cheap, abundant, and renewable energy source, it is poorly utilized. The growing demand for cheap and renewable energy sources has led to substantial research effort to invent low-cost and highly-efficient photovoltaic materials and devices. third generation solar cells, halide perovskite solar cells (PSCs) have a great

Address correspondence to Shibin Li, shibinli@uestc.edu.cn; Zhi David Chen, zhichen@uestc.edu.cn/zhichen@engr.uky.edu

potential for highly efficient solar energy conversion. As ideal light harvesters, the family of perovskite materials are gifted with various attractive optoelectronic characteristics, including high absorption coefficient, tunable bandgap, long carrier diffusion length etc. Among various perovskite materials, methylammonium lead iodide (MAPbI$_3$), with a bandgap of about 1.5eV and an absorption spectrum up to 800 nm, has been extensively studied as a light harvester in solar cells. Following a rapid surge of development, solution processed MAPbI$_3$ has boosted the power conversion efficiency (PCE) of PSCs over 20% [1-18].

The state-of-the-art perovskite solar cells consist of a mesoporous TiO$_2$ electron transport material (ETM), a MAPbI$_3$ light-absorption layer and a spiro-OMeTAD hole transport layer. However, it is well known that the electron mobility of zinc oxide (ZnO) is substantially higher than that of TiO$_2$. ZnO is thus considered as an ideal alternative to TiO$_2$ for electron transport layer in perovskite solar cells. Large efforts have been devoted to developing the ZnO nanostructure based PSCs. Liu et al. reported PSCs with PCEs of 13.5% and 15.7% by using ZnO nanoparticles as ETM [19]. A perovskite solar cell using ZnO nanorods (NRs) as ETM has yielded a PCE of 11% [20]. With Al-doped ZnO interfacial modification, the PCE of ZnO NRs-based PSCs was impressively enhanced up to 10.7% [21]. Khalid and coworkers reported electron rich, nitrogen doped ZnO NRs-based PSCs with the highest PCE of 16.1% so far [22]. The above mentioned results have demonstrated that ZnO based nanostructures could be a competent candidate to replace TiO$_2$. However, why is the PCE of ZnO ETM based PSCs still inferior to the mesostructured TiO$_2$ based PSCs? It was reported that the efficiency losses originate from rapid carrier recombination at the interfaces, especially the interface between ZnO NRs and perovskite [23-25]. Therefore, it is of critical importance to find a way to passivate the defects at the interface between the oxide ETM and the perovskite material. In this paper, we report a new approach to passivate the interfacial defects between ZnO NRs and perovskite using atomic layer deposition (ALD). It was reported that the ALD-Al$_2$O$_3$ film was used for passivation of silicon solar cells [26]. Al$_2$O$_3$ films were deposited by ALD at the interfaces either between perovskite and HTM or between HTM and the Ag electrode for isolation of solar cells from moisture in air [27]. ALD-Al$_2$O$_3$ films were also used as encapsulation layers for protection of solar cells from moisture and oxygen [28]. ALD-Al$_2$O$_3$ and ALD-TO$_2$ layers were deposited to passivate the surface defect of TiO$_2$ and ZnO ETM for PSCs [29,30]. In this work, we demonstrate ALD-Al$_2$O$_3$ monolayers can remarkably suppress the surface defects of ZnO NRs. The average PCE (PCE$_{avg}$) of ZnO NRs-based PSCs is impressively improved from 10.33% to 15.06%. The attained best efficiency of PSCs is 16.08%, which is the state-of-the-art efficiency of ZnO based PSCs [22]. The interface engineering proposed in this work can also be used to passivate defects in other types of perovskite solar cells.

2 Results and Discussion

2.1 Preparation and Optimization of ZnO NRs

Before ZnO NRs were synthesized, a ZnO seed layer (30nm) was prepared by magnetron sputtering at room temperature on the fluorine-doped tin oxide (FTO) glass substrate. It has been demonstrated that the photovoltaic performance and interfacial electronic behavior of the PSCs based on 1D nanostructured ETM with surface-decorated MAPbI$_3$ nanocrystals strongly depend on the length of the oxide arrays [20-22]. In this study, the ZnO NRs were synthesized by the hydrothermal method. We assume that the length of NRs depends directly on the growth time at a fixed precursor concentration. The influence of growth time on the length of ZnO NRs was

examined using a precursor solution (35mM) at a fixed concentration. ZnO NRs were grown at 90°C for 0.5h, 1h, 2h and 3h (correspondingly marked as A, B, C, D). The length was determined by cross-section SEM as shown in Figure 1 (a)-(d). Consequently, the average lengths of NRs for A, B, C, and D are 342, 910, 1730 and 2000 nm, respectively. It is worth to noting that the growth time only affects the lengths of NRs but their diameters [31,32]. The diameter of nanorods is controlled by the precursor concentration as suggested in the SEM images shown in Figure S1 (Supporting Information). In this study, it is difficult to produce the same thickness of perovskite capping layer on the ZnO NRs with different lengths. For NRs with the average lengths of 342, 910, 1730 and 2000 nm, we used PbI_2 solutions with doses of 10, 20, 30 and 40μl to prepare perovskite capping layers on ZnO NRs as shown in the cross-section SEM images of Figure 1 (A)-(D). As shown in Figure 2S, the passivation of ALD-Al_2O_3 monolayers shows negligible effects on the grains size, and good quality of perovskite films are prepared by using mixture solution of DMF: DMSO=7:3. After synthesis of nanorods, the samples were annealed in O_2 at 500 °C for 30 minutes to improve the quality of the seed layer and nanorods. The results of XRD measurements shown in Figure S3 confirm that the seed layer and nanorods are completely crystallized after annealing. Only one strong peak ascribed to the diffraction from (0002) facet of wurtzite ZnO is observed. The (0002) diffraction peak indicates that the ZnO seed layer and nanorods are crystallized in wurtzite structure with c-axis preferred orientation, which favors high electron mobility. Our previous
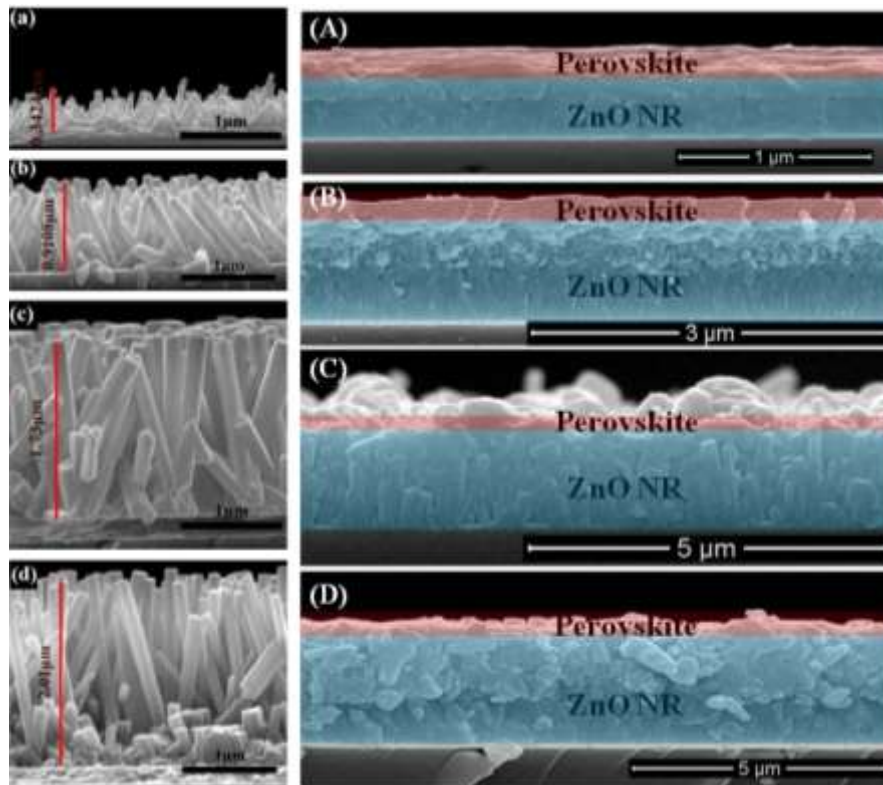

Figure 1 SEM cross section view of ZnO nanorods fabricated for different reaction time: (a) 0.5 h, (b) 1 h, (c) 2 h, (d) 3 h; SEM cross section view of perovskite solar cells (Marked as Sample A, B, C, and D corresponding to the lengths of ZnO NRs) fabricated using ZnO nanorods with different lengths.

work demonstrated that electrons generated in the bulk perovskite are easily conducted to the FTO electrode through the ZnO NRs electron transport layer because high c-axis preferred-orientation ZnO NRs are perpendicular to the FTO substrate [33]. However, the XRD results obtained from the unannealed ZnO showed different crystal orientations, for instance, (100), (103), (112) and (201). Furthermore, the dense and completely crystallized ZnO seed layer also plays a significant role as a blocking layer that prevents direct contact between FTO and perovskite, which dramatically suppresses carrier recombination.

2.2 Effect of Length of ZnO NRs on PCE

Figure 2 exhibits fabrication processes of ALD interface engineering of PSCs based on ZnO NRs. As we have verified that the perovskite capping layer plays a crucial role as a protection layer to prevent direct contact between the ZnO NRs and the spiro-MeOTAD hole transporting material [34,35]. The configuration of a ZnO NRs-based PSC and energy bands/levels of the layers in the cell are shown in Figure 3 (a) and (b), respectively. The diagrams were drawn with the assumption of

vacuum level alignment [17]. Meanwhile, the individual energy levels of various device components are relative to the vacuum level. Additionally, the perovskite capping layer captures photons efficiently and thus results in a superior light harvesting efficiency. A similar concern in mesoporous TiO_2 based PSCs has also been extensively addressed. The remaining PbI_2 is always an issue for the reproducible performance of PSCs. The performance of PSCs is irreproducible because the ratio of $MAPbI_3$ to PbI_2 is not the same from batch to batch. As shown in the XRD patterns of Figure 3 (c), no residual PbI_2 is observed in both Samples A and B, which suggests a full conversion of PbI_2 to $MAPbI_3$. More perovskite is loaded on longer nanorods, and the XRD results of Sample B indicate stronger perovskite peaks of (110), (112), (220), (310) and (312). Sample D shows much stronger diffraction peak of PbI_2 than that of Sample C. The result demonstrates that the amorphous and uniform PbI_2 can be fully converted to perovskite crystals for samples A and B with shorter ZnO NRs. For Samples C and D, the remaining PbI_2 cannot be fully converted to perovskite crystals even prolonging the dipping time to 1 hour.
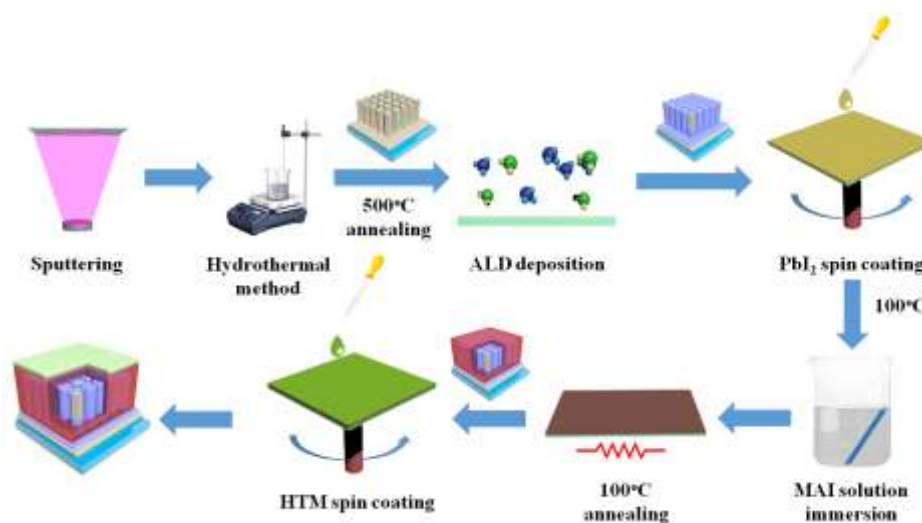

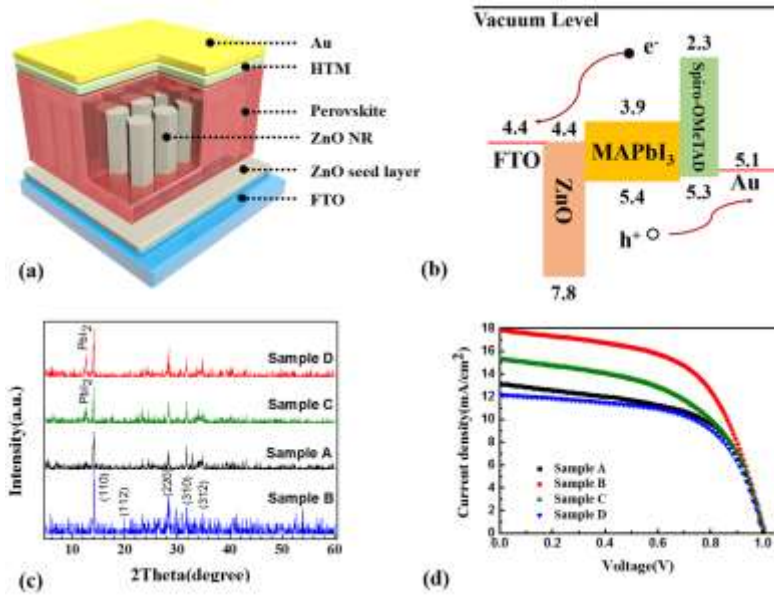**Figure 2** Flow chart of the experiment processes.

Figure 3 (a) Device architecture; (b) Energy-level diagram; (c) XRD patterns of perovskite prepared with different lengths of ZnONRs, Samples A, B, C, and D are corresponding to the lengths of 342, 910, 1730, and 2000 nm; (d) J-V curves of PSCs based on different lengths of ZnO NRs. Samples A, B, C, and D are corresponding to lengths of 342, 910, 1730, and 2000 nm.

As shown in Figure S4 (a), the perovskite film was peeledpeeled off after 1-hour dipping time. In Figure S4 (b), we also observed strong absorption peak around 775 nm ascribed to perovskite, indicating completed conversion of PbI_2 to $MAPbI_3$ with dipping time of 1 minute with the optimized length of ZnO NRs. The result is consistent with the sequential deposition of perovskite reported by Grätzel et al [4]. The capping layer of crystallized perovskite on the top of ZnO NRs prevents the PbI_2 that is left among nanorods from conversion to $MAPbI_3$, resulting in more remaining PbI_2 in Samples C and D with longer nanorods that are able to load more PbI_2. The partial conversion of PbI_2 leads to a $MAPbI_3$-PbI_2 mixture as well as a hardly controllable amount of remaining PbI_2 [36]. As shown in Figure 3 (d) and Table 1, the performance of PSCs based on as-grown ZnO NRs obviously depends on the length of NRs. The PSC (Sample A) based on ZnO NRs with a length of 342 nm exhibits PCE of 7.70%, Jsc of 13.11 mA/cm², FF of 58.67 % and Voc of 1.00V. As the length of nanorods increases, the PCE and Jsc of Sample B increase to 10.38% and 17.85 mA/cm². For

perovskite capping layers with similar thicknesses, the length-related improvement of performance is owing to the longer ZnO NRs, which allows loading more perovskite, resulting in more light absorption. It is reasonable that both the light harvesting and charge generation efficiency increase with the increase of ZnO NRs length. However, the performance of Samples C and D degraded as the lengths of ZnO NRs were increased to 1730 and 2000 nm.The increased length raises the transport distance and resistance of photo-generated carriers, leading to more recombination of carriers. Furthermore, for the PSCs with long ZnO NRs, the capping layers make main contribution to light harvest. Therefore, the increment of perovskite among ZnO NRs hardly enhances the performance further.

The above results demonstrate that the PSC based on ZnO NRs with the length of 910 nm (Sample B) exhibits the best performance among the PSCs with different lengths nanorods. The following studies therefore are focused on the performance of PSCs based on ZnO NRs with the length of 910 nm. As shown in Figure S5, the annealing process

Table 1 Performance parameters of PSCs prepared using ZnO NRs of different lengths.

	V_{oc}[V]	J_{sc}[mA/cm^2]	FF[%]	PCE[%]
Sample A	1.00	13.11	58.67	7.70
Sample B	1.01	17.85	57.70	10.38
Sample C	1.01	15.29	53.34	8.22
Sample D	1.00	12.17	60.56	7.38

the PCE of PSCs from 10.38% to 11.72%. The improved quality of ZnO NRs through annealing is essential for fabrication of high efficiency PSCs [37]. Additionally, the perovskite material may make direct contact on FTO through a thin seed layer, leading to a large leakage current and hence reduced Voc. The Voc increases with the thickness of the seed layer owing to the suppressed leakage current. Therefore, all the PSCs with seed layers of similar thicknesses exhibit similar Voc, because the open circuit voltage is mainly dependent on the thickness of ZnO seed layer. The single crystalline ZnO ETM obtained by annealing is c-axis orientation as well as perpendicular to the FTO substrate, providing a direct carrier pathway. The PCE of devices is therefore significantly improved due to efficient electron collection by the Au electrode. Meanwhile, the as-grown ZnO NRs are polycrystalline, which may disturb the transport of free electrons in ZnO ETM. The disturbing effect increases scattering of free electrons in ZnO ETM, leading to performance deterioration of PSCs [38-41].

2.3 Interface Engineering of PSCs Using ALD

As indicated above, the enhancement of performance is possible for the PSCs based on single crystal ZnO NRs because the trap states are suppressed to a certain extent. To further investigate the influence of interface engineering on the performance of PSCs, ALD-deposited Al$_2$O$_3$ monolayers were coated on the surface of the annealed ZnO NRs to suppress the defects, resulting in enhanced PCE of solar cells. As displayed in Figure S6, the linear increment of

thickness with the number of ALD cycles ensures high-quality passivation of ZnO NRs by ALD-Al$_2$O$_3$. In addition, Al element is chemically active, and thus can be easily oxidized in the water cycle. The linear growth demonstrates that it is a conformal deposition of one-atomic-layer by one-atomic-layer. On considering both fully oxidation and conformal deposition, the Al$_2$O$_3$ film quality is assured. This is also suggested in References [42-44]. The energy levels of the interface engineered solar devices include the bandgap of ALD-Al$_2$O$_3$ monolayers as shown in the inset of Figure 4 (a). As the number of ALD-Al$_2$O$_3$ monolayers increases, the wide bandgap of Al$_2$O$_3$ could block tunneling of free electrons from MAPbI$_3$ to ZnO, which degrades the PCE of solar devices. As a result, there is a trade-off between the PCE enhancement and degradation induced by ALD- Al$_2$O$_3$ passivation. Figure 4 (a) shows that the performance of ZnO NRs based PSCs is not only significantly enhanced by the ALD-Al$_2$O$_3$ coating but also depending on ALD cycles. As summarized in Table 2, one cycle ALD-Al$_2$O$_3$ coating on the ZnO NRs causes the PCE improvement from 11.72% to 12.62%, the Jsc from 19.65 mA/cm^2 to 20.90 mA/cm^2, the FF from 58.46% to 59.13%, and the Voc from 1.020V to 1.021V. To investigate the influence of ALD-Al$_2$O$_3$ on the surface electron trap density of ZnO, we measured the I-V curves of ZnO with contacts, as shown in Figure 4 (b). The log-log plot of I-V curves demonstrate that the current increases linearly with voltage at the lower bias voltage region. At the higher bias voltage region, the current increases at a much higher slope. The transition point is the ohmic to trap filled limit transition point (V_{TFL}) and related to the trap density (Nt) linearly[45].
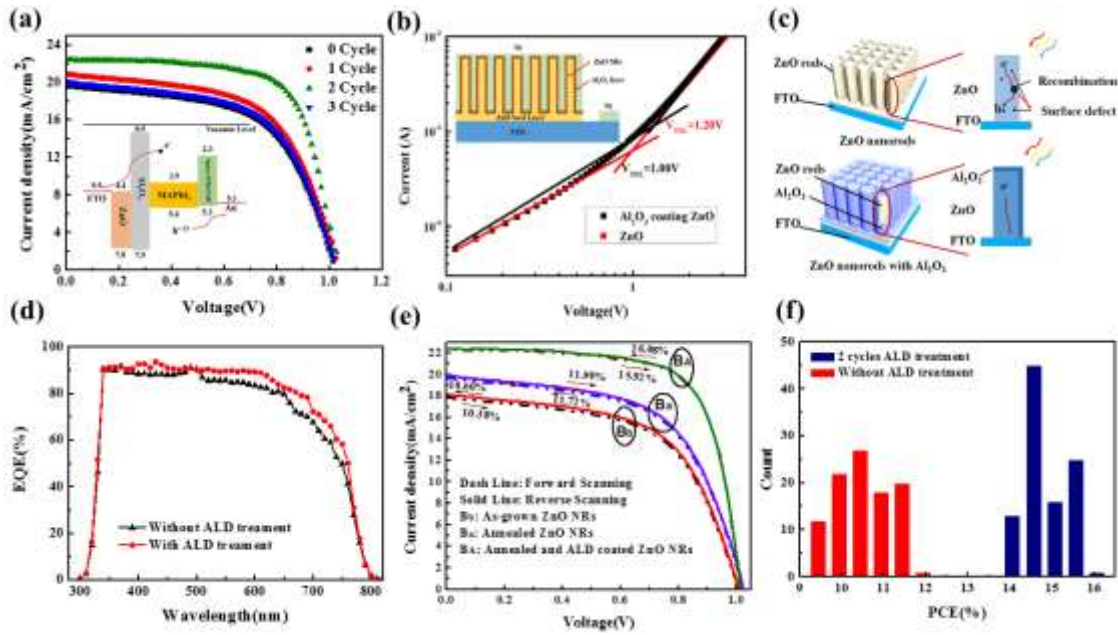
Figure 4 (a) Dependent of J-V curves on cycles of ALD-Al$_2$O$_3$, Inset: Energy-level diagram of PSCs based on Al$_2$O$_3$ coating; (b) Log-log plot curves of ZnO ETM; (c) Schematic diagram of ALD-Al$_2$O$_3$ on ZnO NRs showing suppression of recombination on the surface; (d) EQE spectra of the best device fabricated without ALD cycle and that with two ALD cycle treatment; (e) J-V curves both in forward (dash line) and reverse (solid line) scanning directions of PSCs fabricated using 910 nm length of as-grown ZnO NRs, annealed ZnO NRs, and annealed ZnO NRs with ALD-Al$_2$O$_3$; (f) Reproducibility of annealed ZnO NRs-based PSCs fabricated with two ALD cycles and without ALD cycles.

Table 2 Dependence of performance of PSCs on ALD-Al$_2$O$_3$ cycles. The PSCs based on ZnO NRs with length of 910 nm.

ALD cycles	Voc[V]	Jsc[mA/cm^2]	FF [%]	PCE [%]
0 cycle	1.020	19.65	58.46	11.72
1cycle	1.021	20.90	59.13	12.62
2 cycle	1.023	22.42	71.43	16.08
3 circle	1.018	20.05	58.69	11.98

The value of V$_{TFL}$ increases as electron traps. The values of V$_{TFL}$ can be estimated from the I-V curves. The V$_{TFL}$ of devices based on ZnO (1.20 V) is higher than that based on ZnO with two cycles of ALD-Al$_2$O$_3$ (1.00V). According to the relation between surface traps and V$_{TFL}$, the density of surface electron traps in the ZnO is much higher than that of the in the ALD-Al$_2$O$_3$ coated ZnO. The results show evidence of the reduction of surface defects of ZnO by the passivation of ALD-Al$_2$O$_3$ monolayers. As shown in Figure 4 (c), the inferior performance of ZnO NRs based PSCs is due mainly to trap states derived from defects on the surface of ZnO NRs. In perovskite solar cells, the generated free carriers from MAPbI$_3$ dissociate mainly at the interface of ETM/MAPbI$_3$. The photogenerated holes may be captured easily by the defect induced trap on the surface of ZnO NRs. The ALD-Al$_2$O$_3$

coating functions not only as a defect passivation layer, but also as a blocking layer to obstruct the photogenerated holes into the ETM. Furthermore, the ALD-Al_2O_3 coating leads to surface band bending and accelerates the separation of photogenerated carriers, which enhances the internal quantum efficiency (IQE)and results in the performance improvement. As a result, after two cycles of ALD-Al_2O_3 being deposited at the interface of ZnO NRs and the perovskite light harvester, the performance of PSCs is further enhanced. ALD-Al_2O_3 coating of two cycles on the ZnO NRs improves the PCE from 12.62 % to 16.08%, the Jsc from 20.90 mA/cm^2 to 22.42 mA/cm^2, the FF from 59.13% to 71.43%, and the Voc from 1.021V to 1.023V. It is confirmed that the implemented annealing process remarkably reduces the surface defects on ZnO. As a result, only two cycles of ALD-Al_2O_3 are enough to heal the defects on the surface of ZnO ETM in PSCs. The performance of PSCs based on annealed ZnO NRs deteriorates because the photogenerated electrons are blocked by ALD-Al_2O_3 deposited over two cycles as mentioned above. The external quantum efficiency (EQE) spectrum shown in Figure 4 (d) indicates the onset of photocurrent at 800nm, which is consistent with the reported bandgap of MAPbI$_3$ (1.55eV) [11,46]. Although both EQE spectra show similar shapes, the two-cycle ALD-Al_2O_3 coating on annealed ZnO NRs attains obviously higher EQE than that without ALD-Al_2O_3 coating on ZnO NRs. Especially, without ALD-Al_2O_3 coating, in the wavelength from 500 to 750nm, surface defects on ZnO NRs lead to efficiency loss. The performance of PSCs based on the ALD interface engineering is

dramatically improved by suppressing the surface defects. As suggested by previous reports, the poor interface between the perovskite and the oxide ETM contributes majorly to the J-V hysteresis in MAPbI$_3$ perovskite solar cell [47,48]. The J-V characteristics in both forward and reverse scanning directions, shown in Figure 4 (e), demonstrate the best performance of PSCs based on as-grown, annealed and 2-cycle ALD-Al_2O_3 monolayer coated ZnO NRs (910nm). The J-V curves of PSCs based on as-grown ZnO NRs show that the PCE from forward scanning direction (PCE$_{fwd}$) is 10.38%, which is lower than that (10.60%) from reverse scanning direcition (PCE$_{rev}$). The PCE$_{fwd}$ of 11.72% obtained from the PSC based on annealed ZnO NRs is slightly lower than the PCE$_{rev}$ of 11.90% as well. After 2-cycle ALD-Al_2O_3 monolayers applied on the annealed ZnO NRs, the J-V curves of devices exhibit negligible hysteresis with the best PCE$_{fwd}$ of 16.08%. Because of ZnO thermal annealing and ALD-Al_2O_3 coating ZnO NRs, the best solar cell exhibits negligible hysteresis nature due to less interface defects between MAPbI$_3$ and ZnO ETM. Reproducibility is essential for commercial production of large area PSCs, and we fabricated 100 solar cell devices based on annealed ZnO NRs and annealed ZnO NRs passivated by two-cycle ALD-Al_2O_3, respectively. The histogram shown in Figure 4 (f) exhibits the distribution of efficiencies of the devices fabricated with/without ALD-Al_2O_3 interface engineering. The statistical data shown in Table 3 suggests that the PSCs fabricated using ALD-Al_2O_3 yield lower standard deviations (±0.49) and higher average PCEavg of 15.06%. However, the PSCs fabricated without ALD-Al_2O_3

Table 3 Standard deviation of efficiency of ZnO NRs-based PSCs, 100 devices were fabricated for each group.

	Device Number	Standard Deviation	PCE$_{min}$[%]	PCE$_{avg}$[%]	PCE$_{max}$[%]
2 cycles ALD	100	0.49	14.20	15.06	16.08
Without ALD	100	0.69	9.06	10.33	11.72

exhibit higher standard deviations (±0.69) and lower PCE$_{avg}$ of 10.33%. The results demonstrate that ALD-Al$_2$O$_3$ on ZnO NRs also results in high reproducibility of PSCs.

To further confirm that the PCE improvement of PSCs is ascribed to the ALD-Al$_2$O$_3$ interface engineering, the full-scan XPS spectra of ZnO NRs were obtained. As show in Fig. 5 (a), the existence of Zn, O, C elements are confirmed in both ZnO NRs. The XPS peak of Zn 2p 3/2 centered at 1022eV is for ZnO NRs. The Zn 2p XPS peaks of two ZnO NRs samples are corresponding to crystal lattice zinc of ZnO [49]. Comparing the full-scan XPS spectra of the two samples, a weak, but distinct Al 2s peak at 125eV is ascribed to ALD- Al$_2$O$_3$. The C 1s peak at 285eV is ascribed to the carbon contamination from the organics used to prepare ZnO NRs [49]. As shown in Figure 5 (b) and (c), the O 1s XPS peaks of annealed ZnO NRs and annealed ZnO NRs with ALD-Al$_2$O$_3$ are decomposed into two components by fitting with the Gaussian function that centered at 530 and 531eV, respectively. The peak at a lower binding energy is attributed to O^{2-} ions in ZnO crystal lattice, and the peak at a higher binding energy is associated with O^{2-} ions in oxygen-deficient regions within the matrix of ZnO [49,50]. The peak centered at 531 eV ascribed to oxygen vacancies generated by loosely bound oxygen on the surface of ZnO NRs. The atomic percentages of O^{2-} ions in oxygen-deficient regions are reduced from 42.1% to 28.4% owing to passivation of ALD-Al$_2$O$_3$ on ZnO NRs. The XPS results indicate that the ALD-Al$_2$O$_3$ coating on ZnO NRs apparently suppresses the peak intensity of O2- ions because a certain amount of oxygen vacancies on the surface of ZnO NRs are repaired. Figure 5 (d) shows the photoluminescence property of ZnO NRs measured at the room temperature. The PL spectra clearly indicate that the ZnO NRs exhibit a near band emission around 380 nm and a broad visible emission (450-650 nm) that is usually associated with oxygen defects. Among the different defects proposed to explain the visible PL emission, oxygen vacancies are considered to be the most prominent one [51,52]. The intensity of UV emission is obviously enhanced and that of visible emission is suppressed to some extent by coating
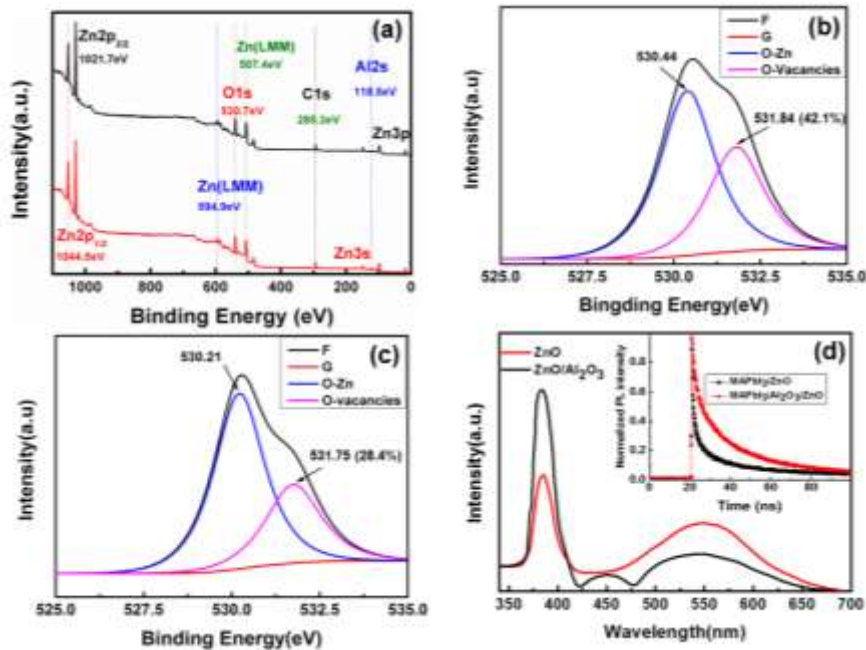

Figure 5 (a) Full scan XPS of ZnO NRs (black) and ZnO NRs with ALD-Al2O3 (red); (b) O 1s XPS spectra of ZnO NRs; (c) O 1s XPS spectra of ZnO NRs with ALD-Al$_2$O$_3$; (d) PL spectra of ZnO NRs, insect: time-resolved PL of MAPbI$_3$ on ZnO NRs.

ZnO NRs with ALD-Al_2O_3. Furthermore, the time-resolved PL shown in the inset of Figure 5 (d) clearly shows an improvement in emission decay time, which supports that the ALD-Al_2O_3 monolayers on ZnO NRs suppresses the surface recombination of $MAPbI_3$, and thus the passivation enhances the PCE of PSCs. The obtained XPS and PL spectra are also consistent with the results from previous reports [29,45,51]. The enhancement of PCE of PSCs exhibited in Figure 4 (e) is confirmed by the results from XPS and PL measurements shown in Figure 5.

3 Conclusion

High performance PSCs based on interface engineering of ZnO NRs are successfully fabricated. The residual PbI_2 in $MAPbI_3$ crystals on ZnO NRs was eliminated by utilizing the mixture solvent of DMSO and DMF (VDMF: VDMSO =7:3) for PbI_2 to suppress the crystallization rate of PbI_2. The full conversion of PbI_2 to $MAPbI_3$ enables a uniform surface morphology of perovskite film, which ensures reproducibility of PSCs. The performance of PSCs was significantly improved by the ALD interface engineering for surface defect passivation of ZnO NRs. The PSCs based on annealed ZnO NRs passivated by ALD-Al_2O_3 exhibit the best PCE of 16.08% and the average PCE of 15.06%. We suggest that ALD-grown monolayers provide a new pathway for passivation of defects for PSCs.

4 Experimental

4.1 Growth of ZnO NRs and fabrication of PSCs

The ZnO NRs were grown based on a two-step method reported elsewhere [20, 21]. A thin ZnO film (30 nm) seed layer was prepared on a FTO coated glass. The well-arranged ZnO NRs were fabricated by immersing the preseeded samples into a solution of $Zn(NO_3)_2$ and hexamethylenetetramine(HMT) at 95 ^oC. The Al_2O_3 monolayers were deposited by ALD on the prepared ZnO NRs. The PSCs were fabricated using ZnO NRs by a two-step method in a nitrogen-filled glove box (<1 ppm O_2 and H_2O). The PbI_2 (460 mg/mL) was dissolved in a mixture solution of DMF: DMSO=7:3 at 70 ^oC. Following the spin-coating of the dissolved PbI_2 solution on ZnO NRs at 5000rpm for 30s, the sample was dipped into a MAI solution for 1min (MAI was dissolved in 2-propanol under stirring at a concentration of 10mg/mL). Consequently, the $MAPbI_3$ perovskite layer was produced by heating the sample at 100 ^oC for 5 min. The hole transporting layer was deposited by spin-coating the spiro-OMeTAD solution at 4000 rpm for 30 s. Finally, 80 nm of gold was prepared by e-beam evaporation on the top of the devices as a back contact.

4.2 Measurement and Characterization

The measurement of current-voltage curves was carried out under AM 1.5 simulated sunlight (Newport, Oriel Sol3A Class Simulator, calibrated using an NREL-calibrated Si solar cell) with a Keithley 2400. The EQE measurements were performed employing a 150 W Xe lamp coupled with a monochromator controlled by a mputer. The photocurrent was measured using an optical power meter 70310 from Oriel Instruments, using a Si photodiode to calibrate the system. Surface morphology, cross-sectional scanning electron images of the NRs, and complete solar cell structures were obtained using field emission SEM (FEI-Inspect F50, Holland). X-ray diffraction measurements were performed using a Bede D1 system with Cu Kα radiation. The UV-vis absorption spectra of ZnO NRs/perovskite films were measured using an ultraviolet-visible (UV–vis) spectrophotometer (Schimadzu UV-3101 PC). XPS characterizations were carried out by using an instrument made by Thermo Scientific (Escalab 250Xi).

Acknowledgements

Electronic Supplementary Material: Supplementary material (further details of top view of ZnO NRs via SEM; XRD patterns of as-grown and annealed ZnO NRs; Properties of perovskite material and devices, linear growth of Al_2O_3) is available in the online version of this article at xxxxx

References

[1] Chen, L.; Tang, F.; Wang, Y.; Gao, S.; Cao, W.; Cai, J.; Chen, L. Facile preparation of organometallic perovskite films and high-efficiency solar cells using solid-state chemistry. *Nano Research* **2015**, *8*, 263-270.

[2] Kim, H. S.; Lee, C. R.; Im, J. H.; Lee, K. B.; Moehl, T.; Marchioro, A.; Moon, S.; Humphry-Baker, R.; Yum, J.; Moser, J. E.; Grätzel, M.; Park, N. G. Lead iodide perovskite sensitized all-solid-state submicron thin film mesoscopic solar cell with efficiency exceeding 9%. *Sci. Rep.* **2012**, *2*, 591.

[3] Lee, M. M.; Teuscher, J.; Miyasaka, T.; Murakami, T. N.; Snaith, H. J. Efficient hybrid solar cells based on meso-superstructured organometal halide perovskites. *Science* **2012**, *338*, 643-647.

[4] Burschka, J.; Pellet, N.; Moon, S. J.; Humphry-Baker, R.; Gao, P.; Nazeeruddin, M. K.; Grätzel, M. Sequential deposition as a route to high-performance perovskite-sensitized solar cells. *Nature* **2013**, *499*, 316-319.

[5] Liu, M.; Johnston, M. B.; Snaith, H. J. Efficient planar heterojunction perovskite solar cells by vapour deposition. *Nature* **2013**, *501*, 395-398.

[6] Ball, J. M.; Lee, M. M.; Hey, A.; Snaith, H. J. Low-temperature processed meso-superstructured to thin-film perovskite solar cells. *Energy Environ. Sci.* **2013**, *6*, 1739-1743.

[7] Dualeh, A.; Tétreault, N.; Moehl, T.; Gao, P.; Nazeeruddin, M. K.; Grätzel, M. Effect of annealing temperature on film morphology of organic–inorganic hybrid perovskite solid‐state solar cells. *Adv. Funct. Mater.* **2014**, *24*, 3250-3258.

[8] Yella, A.; Heiniger, L. P.; Gao, P.; Nazeeruddin, M. K.; Grätzel, M. Nanocrystalline rutile electron extraction layer enables low-temperature solution processed perovskite photovoltaics with 13.7% efficiency. *Nano Lett.* **2014**, *14*, 2591-2596.

[9] Green, M. A.; Ho-Baillie, A.; Snaith, H. J. The emergence of perovskite solar cells. *Nat. Photonics* **2014**, *8*, 506-514.

[10] Yan, W.; Li, Y.; Li, Y.; Ye, S.; Liu, Z.; Wang, S.; Bian, Z.; Huang, C. Stable high-performance hybrid perovskite solar cells with ultrathin polythiophene as hole-transporting layer. *Nano Research* **2015**, *8*, 2474-2480.

[11] Jeon, N. J.; Noh, J. H.; Kim, Y. C.; Yang, W. S.; Ryu, S.; Seok, S. I. Solvent engineering for high-performance inorganic–organic hybrid perovskite solar cells. *Nat. Mater.* **2014**, *13*, 897-903.

[12] Zhou, H.; Chen, Q.; Li, G.; Luo, S.; Song, T. B.; Duan, H. S.; Hong, Z.; You, J.; Liu, Y.; Yang, Y. Interface engineering of highly efficient perovskite solar cells. *Science* **2014**, *345*, 542-546.

[13] Yang, W. S.; Noh, J. H.; Jeon, N. J.; Kim, Y. C.; Ryu, S.; Seo, J.; Seok, S. I. High-performance photovoltaic perovskite layers fabricated through intramolecular exchange. *Science* **2015**, *348*, 1234-1237.

[14] Yin, X.; Guo, Y.; Xue, Z.; Xu, P.; He, M.; Liu, B. Performance enhancement of perovskite-sensitized mesoscopic solar cells using Nb-doped TiO_2 compact

layer. *Nano Research* **2015**, *8*, 1997-2003.

[15] Bi, D.; Tress, W.; Dar, M. I.; Gao, P.; Luo, J.; Renevier, C.; Schenk, K.; Abate, A.; Giordano, F.; Baena, J. P. C.; Decoppet, J. D.; Zakeeruddin, S. M.; Khaja, M.; Grätzel, M. Hagfeldt, A. Efficient luminescent solar cells based on tailored mixed-cation perovskites. *Science advances* **2016**, *2*, e1501170.

[16] Zuo, F.; Williams, S. T.; Liang, P. W.; Chueh, C. C.; Liao, C. Y.; Jen, A. K. Y. Binary‐Metal perovskites toward high‐performance planar‐heterojunction hybrid solar cells. *Adv. Mater.* **2014**, *26*, 6454-6460.

[17] Chueh, C. C.; Li, C. Z.; Jen, A. K. Y. Recent progress and perspective in solution-processed Interfacial materials for efficient and stable polymer and organometal perovskite solar cells. *Energy Environ. Sci.* **2015**, *8*, 1160-1189.

[18] Kumar, M. H.; Dharani, S.; Leong, W. L.; Boix, P. P.; Prabhakar, R. R.; Baikie, T.; Shi, C.; Ding, H.; Ramesh, R.; Asta, M.; Graetzel, M.; Mhaisalkar, S. G.; Mathews, N. Lead‐free halide perovskite solar cells with high photocurrents realized through vacancy modulation. *Adv. Mater.* **2014**, *26*, 7122-7127.

[19] Liu, D.; Kelly, T. L. Perovskite solar cells with a planar heterojunction structure prepared using room-temperature solution processing techniques. *Nature photonics* **2014**, *8*, 133-138.

[20] Son, D. Y.; Im, J. H.; Kim, H. S.; Park, N. G. 11% efficient perovskite solar cell based on ZnO nanorods: an effective charge collection system. *J. Phys. Chem. C* **2014**, *118*, 16567-16573.

[21] Dong, J.; Zhao, Y.; Shi, J.; Wei, H.; Xiao, J.; Xu, X.; Li, D.; Luo, Y.; Meng, Q. Impressive enhancement in the cell performance of ZnO nanorod-based perovskite solar cells with Al-doped ZnO interfacial modification. *Chem. Commun.* **2014**, *50*, 13381-13384.

[22] Mahmood, K.; Swain, B. S.; Amassian, A. 16.1% Efficient Hysteresis‐Free Mesostructured Perovskite Solar Cells Based on Synergistically Improved ZnO Nanorod Arrays. *Adv. Energy Mate.* **2015**, *5*, 1500568.

[23] Bi, D. Q.; Boschloo, G.; Schwarzmüller, S.; Yang, L.; Johansson, E. M.; Hagfeldt, A. Efficient and stable $CH_3NH_3PbI_3$-sensitized ZnO nanorod array solid-state solar cells. *Nanoscale* **2013**, *5*, 11686-11691.

[24] Cheng, Y. H.; Yang, Q. D.; Xiao, J. Y.; Xue, Q. F.; Li, H. W.; Guan, Z. Q.; Yip, H. L.; Tang, S. W. Decomposition of organometal halide perovskite films on zinc oxide nanoparticles. *ACS Appl. Mater. Interfaces* **2015**, *7*, 19986-19993.

[25] Shi, J.; Xu, X.; Li, D.; Meng, Q. Interfaces in perovskite solar cells. *Small* **2015**, *11*, 2472-2486.

[26] Poodt, P.; Lankhorst, A.; Roozeboom, F.; Spee, K.; Maas, D.; Vermeer, A. High‐speed spatial atomic‐layer deposition of aluminum oxide layers for solar cell passivation. *Adv. Mater.* **2010**, *22*, 3564-3567.

[27] Dong, X.; Fang, X.; Lv, M.; Lin, B.; Zhang, S.; Ding, J.; Yuan, N. Improvement of the humidity stability of organic–inorganic perovskite solar cells using ultrathin Al_2O_3 layers prepared by atomic layer deposition. *J. Mater. Chem. A* **2015**, *3*, 5360-5367.

[28] Chang, C. Y.; Lee, K. T.; Huang, W. K.; Siao, H. Y.; Chang, Y. C. High-performance, air-stable, low-temperature processed semitransparent perovskite solar cells enabled by atomic layer deposition. *Chem. Mat.* **2015**, *27*, 5122-5130.

[29] Lee, Y. H.; Luo, J.; Son, M. K.; Gao, P.; Cho, K. T.; Seo, J.; Grätzel, M.; Nazeeruddin, M. K. Enhanced charge collection with passivation layers in perovskite solar cells. *Adv. Mater.* **2016**, *28*, 3966–3972.

[30] Dong, J.; Xu X.; Shi J. J.; Li,D.M.; Luo Y. H.; Meng, Q. B.; Chen Q.; Suppressing Charge Recombination in ZnO-Nanorod-Based Perovskite Solar Cells with Atomic-Layer-Deposition TiO_2. *Chin. Phys. Lett.*, **2015**, *32*, 078401.

[31] Beek, W. J.; Wienk, M. M.; Kemerink, M.; Yang, X.; Janssen, R. A. Hybrid zinc oxide conjugated polymer bulk heterojunction solar cells. *J. Phys. Chem. B* **2005**, *109*, 9505-9516.

[32] Pacholski, C.; Kornowski, A.; Weller, H. Self‐assembly of ZnO: from nanodots to nanorods. *Angew. Chem. Int. Edit.* **2002**, *41*, 1188-1191.

[33] Wang, M.; Li, S.; Zhang, P.; Wang, Y.; Li, H.; Chen, Z. A modified sequential method used to prepare high quality perovskite on ZnO nanorods. *Chemical Physics Letters* **2015**, *639*, 283-288.

[34] H. Li, S. Li, Y. Wang, H. Sarvari, P. Zhang, M. Wang and Z. Chen, *Sol. Energy* **2016**, *126*, 243-251.

[35] Eperon, G. E.; Burlakov, V. M.; Docampo, P.; Goriely, A.; Snaith, H. J. Morphological control for high performance, solution－processed planar heterojunction perovskite solar cells. *Adv. Funct. Mater.* **2014**, *24*, 151-157.

[36] Wu, Y.Z.; Islam, A.; Yang, X. D.; Qin, C. J.; Liu, J.; Zhang, K.; Peng, W. Q.; Han, L. Retarding the crystallization of PbI₂ for highly reproducible planar-structured perovskite solar cells via sequential deposition. *Energy. Environ. Sci.* **2014**, *7*, 2934-2938.

[37] Liang, L.; Huang, Z.; Cai, L.; Chen, W.; Wang, B.; Chen, K.; Bai, H.; Tian, Q.; Fan, B. Magnetron sputtered zinc oxide nanorods as thickness-insensitive cathode interlayer for perovskite planar-heterojunction solar cells. *ACS Appl. Mater. Interfaces* **2014**, *6*, 20585-20589.

[38] Dong, J.; Shi, J.; Li, D.; Luo, Y.; Meng, Q. Controlling the conduction band offset for highly efficient ZnO nanorods based perovskite solar cell. *Appl. Phys. Lett.* **2015**, *107*, 073507.

[39] Tseng, Z. L.; Chiang, C. H.; Wu, C. G. Surface engineering of ZnO thin film for high efficiency planar perovskite solar cells. *Sci. Rep.* **2015**, *5*, 13211.

[40] Nicolaev, A.; Mitran, T. L.; Iftimie, S.; Nemnes, G. A. Optimization of halide perovskite solar cells based on nanocolumnar ZnO. *Sol. Energy Mat. Sol. Cells* **2015**, *158*, 202-208.

[41] Ko, S. H.; Lee, D.; Kang, H. W.; Nam, K. H.; Yeo, J. Y.; Hong, S. J.; Grigoropoulos, C. P.; Sung, H. J. Nanoforest of hydrothermally grown hierarchical ZnO nanowires for a high efficiency dye-sensitized solar cell. *Nano lett.* **2011**, *11*, 666-671.

[42] Frank, M. M.; Chabal, Y. J.; Green, M. L.; Delabie, A.; Brijs, B.; Wilk, G. D.; Ho, M. Y.; Rosa, E. B. O.; Baumvol, I. J. R.; Stedile, F. C. Enhanced initial growth of atomic-layer-deposited metal oxides on hydrogen-terminated silicon. *Appl. Phys. Lett.* **2003**, *83*, 740-742.

[43] Groner, M. D.; Fabreguette, F. H.; Elam, J. W.; George, S. M. Low-temperature Al₂O₃ atomic layer deposition. *Chem. Mater.* **2004**, *16*, 639-645.

[44] Wilson, C. A.; Grubbs, R. K.; George, S. M. Nucleation and growth during Al₂O₃ atomic layer deposition on polymers. *Chem. Mater.* **2005,** *17*, 5625-5634.

[45] Heo, J. H.; You, M. S.; Chang, M. H.; Yin, W.; Ahn, T. K.; Lee, S. J.; Sung, S. J.; Kim, D. H.; Im, S. H. Hysteresis-less mesoscopic CH₃NH₃PbI₃ perovskite hybrid solar cells by introduction of Li-treated TiO₂ electrode. *Nano Energy.* **2015**, *15*, 530-539.

[46] Heo, J. H.; Im, S. H.; Noh, J. H.; Mandal, T. N.; Lim, C. S.; Chang, J. A.; Lee, Y. H.; Kim, H. J.; Sarkar, A.; Nazeeruddin, M. K.; Grätzel, M.; Seok S. Efficient inorganic-organic hybrid heterojunction solar cells containing perovskite compound and polymeric hole conductors. *Nat. Photonics* **2013**, *7*, 486-491.

[47] Jeon, N. J.; Noh, J. H.; Kim, Y. C.; Yang, W. S.; Ryu, S.; Seok, S. I. Solvent engineering for high-performance inorganic–organic hybrid perovskite solar cells. *Nat. Materials* **2014**, *13*, 897-903.

[48] Kim, H. S.; Jang, I. H.; Ahn, N.; Choi, M.; Guerrero, A.; Bisquert, J.; Park, N. G. Control of I–V hysteresis in CH₃NH₃PbI₃ perovskite solar cell. *J. Phys. Chem. Lett.* **2015**, *6*, 4633-4639.

[49] Wang, L.; Feng, L.; Cui, C.; Xu, S.; Liu, J.; Sun, X; Gao, X.; Wang, W. J. Study on the Surface Functionalization of ZnO Nanorods and Their Tunable Electrochem illuminescence Properties. *ECS J. Solid State SC.* **2016**, *5*, R74-R81.

[50] Prasanna, S.; Jayakumar, S.; Kannan, M. D.; Ganesan, V. Dielectric properties of DC reactive magnetron sputtered Al2O3 thin films. *Thin Solid Films* **2012**, *520*, 2689-2694.

[51] Tam, K. H.; Cheung, C. K.; Leung, Y. H.; Djurišic, A.

B.; Ling, C. C.; Beling, C. D.; Fung, S.; Kwok, W. M.; Chan, W. K.; Phillips, D. L.; Ding, L. Defects in ZnO nanorods prepared by a hydrothermal method. *J. Phys. Chem. B*. **2006**, *110*, 20865–20871.

[52] Chen, C.; He, H.; Lu, Y.; Wu, K.; Ye, Z. Surface passivation effect on the Photoluminescence of ZnO nanorods. *ACS applied materials & interfaces* **2013**, *5*, 6354-6359.

Electronic Supplementary Material

Interface engineering of high efficiency perovskite solar cells based on ZnO nanorods using atomic layer deposition

Shibin Li[1],[*]([✉]), Peng Zhang[1], Yafei Wang[1], Hojjatollah Sarvari[2], Detao Liu[1], Jiang Wu[3], Yajie Yang[1], Zhiming Wang[4], Zhi David Chen[1,2],[*]([✉])

[1]School of Optoelectronic Information, University of Electronic Science and Technology of China (UESTC), Chengdu, 610054, China

[2]Department of Electrical & Computer Engineering and Center for Nanoscale Science &Engineering,
University of Kentucky,
Lexington, Kentucky 40506, USA

[3]Department of Electronic and Electrical Engineering, University College London, Torrington Place, London WC1E 7JE, United Kingdom

[4]Institute of Fundamental and Frontier Sciences, University of Electronic Science and Technology of China, Chengdu, 610054, China

Address correspondence to Shibin Li, shibinli@uestc.edu.cn; Zhi David Chen, zhichen@uestc.edu.cn/zhichen@engr.uky.edu

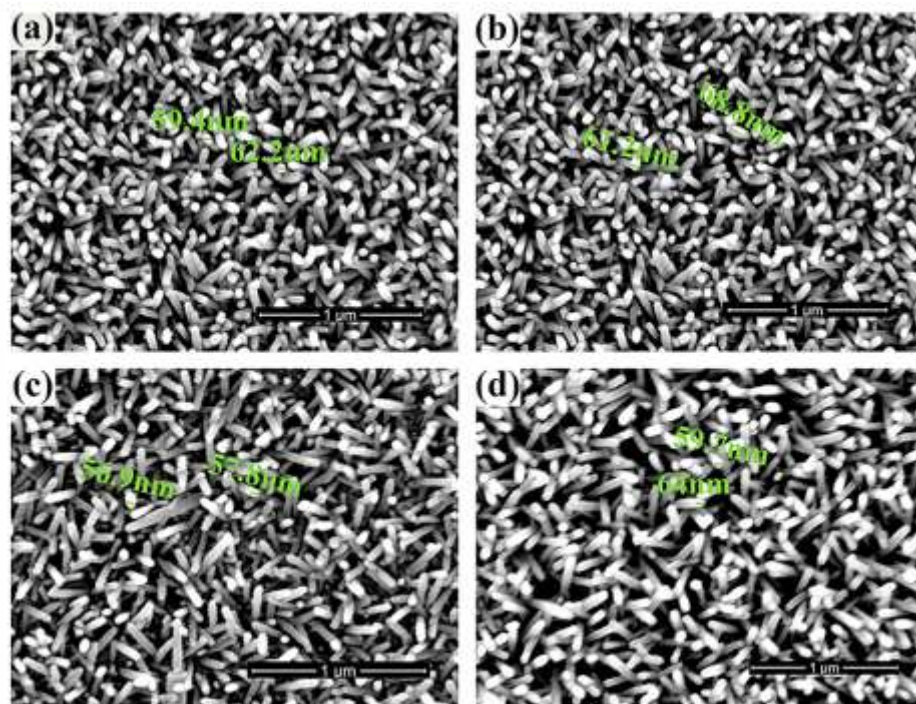**Figure S1** Top view of ZnO NRs prepared at solutions of the same concentration for (a) 0.5 h, (b) 1 h, (c) 2 h, and (d) 3 h.

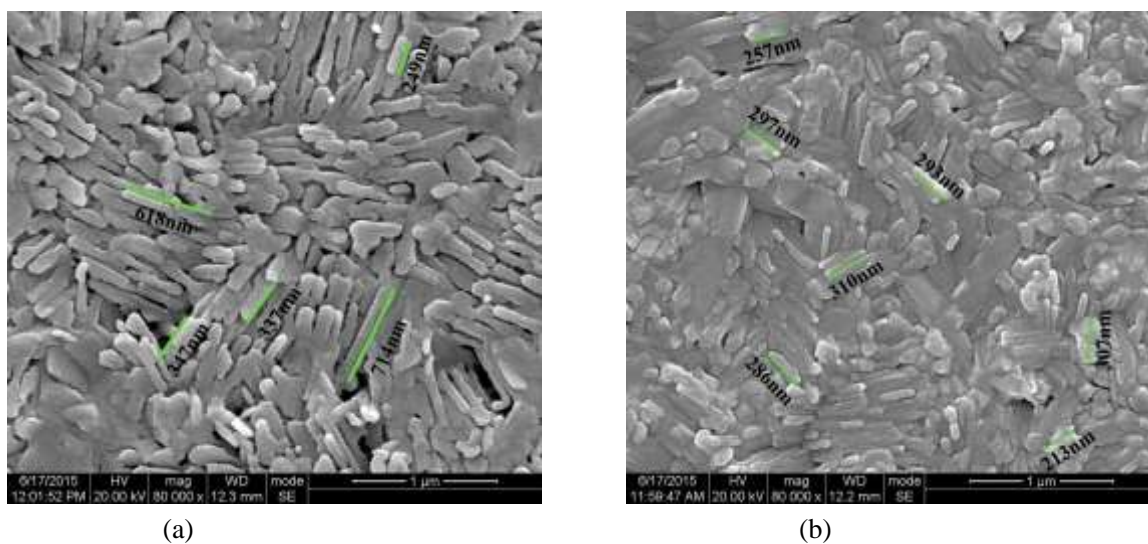(a)   (b)

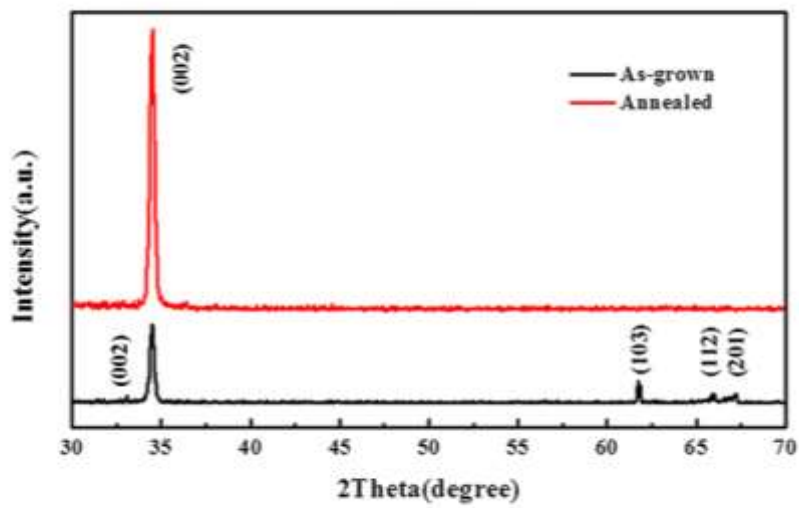**Figure S2** SEM view of perovskite film; (a)MAPbI$_3$/ZnO; (b) MAPbI$_3$/Al$_2$O$_3$/ZnO.

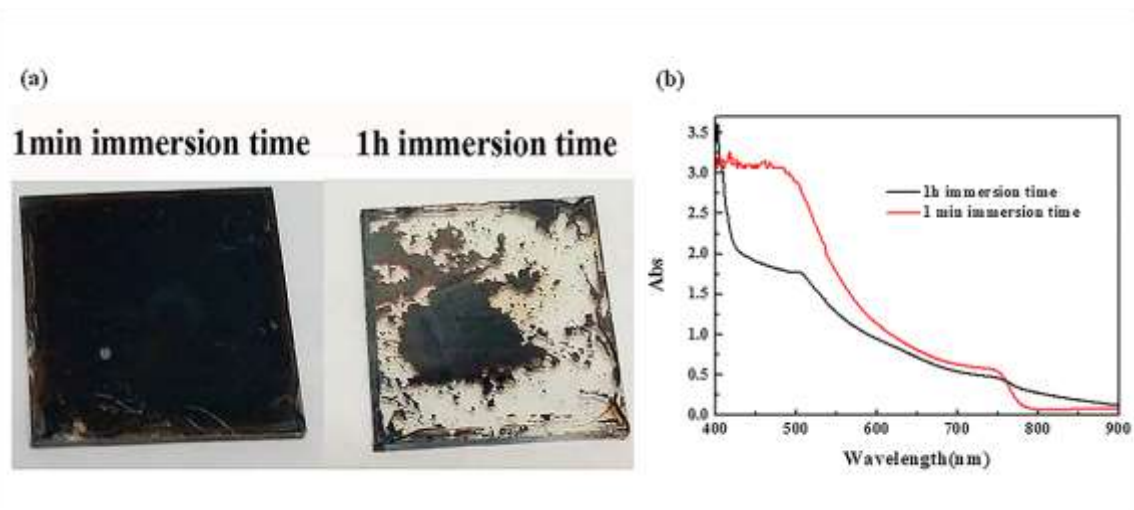**Figure S3** XRD patterns of as-grown ZnO NRs and ZnO NRs annealed at 500 °C for 30 min.

Figure S4 Perovskite film peeling-off as the dipping time exceeds 1 h; (b) UV-VIS absorption curves of perovskite prepared for 1 min and 1 h immersion time.
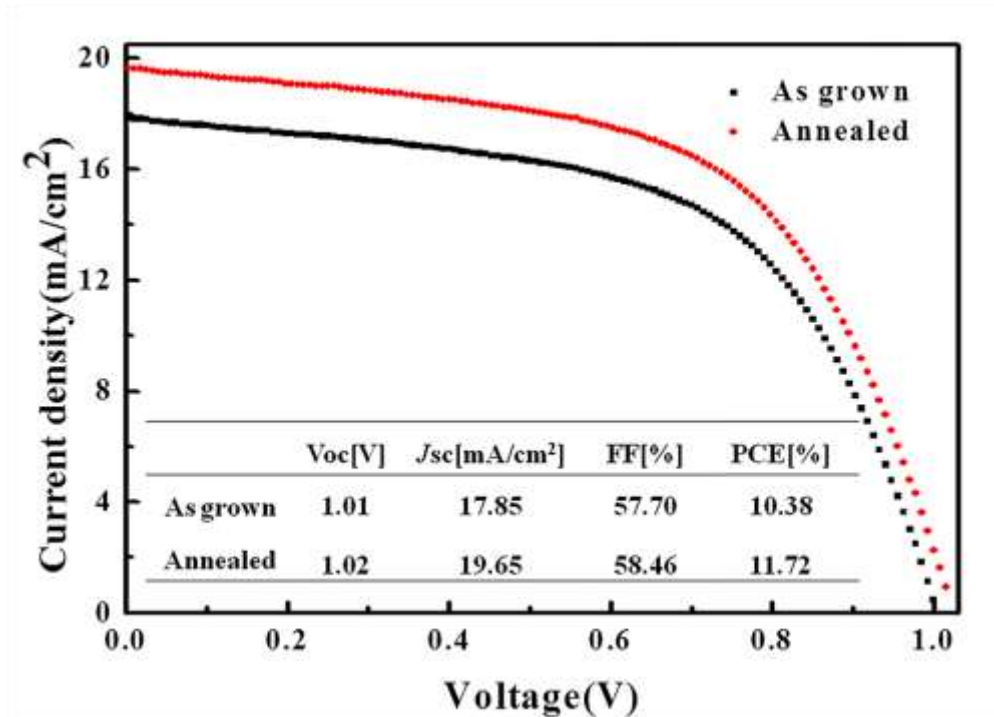
Figure S5 J-V curves of solar cell based on as-grown/annealed ZnO NRs (910 nm). The ZnO NRs used to prepare PSCs were annealed at 500 ℃ for 30 min.
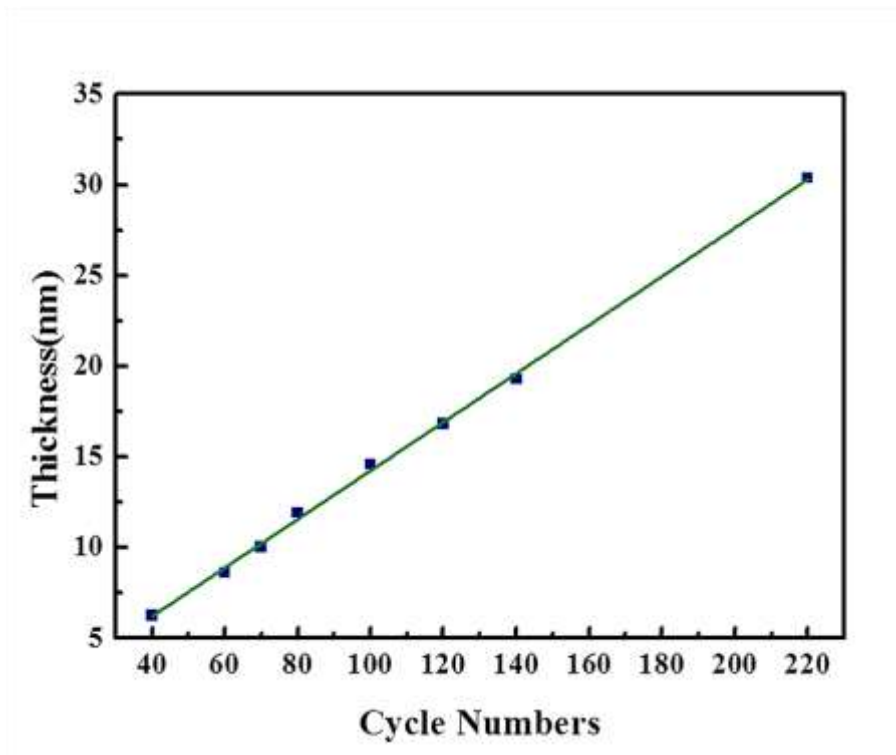

Figure S6 Atomic layer deposition of Al_2O_3 is evidenced by the linear increment of thickness with the ALD cycles.